HHS Public Access

Author manuscript

Neuron. Author manuscript; available in PMC 2019 March 07.

Published in final edited form as:

Neuron. 2018 March 07; 97(5): 1126–1136.e10. doi:10.1016/j.neuron.2018.01.034.

Deconvolution of Voltage Sensor Time Series and Electro-diffusion Modeling Reveal the Role of Spine Geometry in Controlling Synaptic Strength

Jerome Cartailler[1], **Taekyung Kwon**[2], **Rafael Yuste**[2], and **David Holcman**[1,3,*]

[1]Institut de Biologie de l'École Normale Supérieure, 46 rue d'Ulm, 75005 Paris, France

[2]Neurotechnology Center, Depts. Biological Sciences and Neuroscience, Columbia University, New York, NY 10027, USA

SUMMARY

Most synaptic excitatory connections are made on dendritic spines. But how the voltage in spines is modulated by its geometry remains unclear. To investigate the electrical properties of spines, we combine voltage imaging data with electro-diffusion modeling. We first present a temporal deconvolution procedure for the genetically encoded voltage sensor expressed in hippocampal cultured neurons and then use electro-diffusion theory to compute the electric field and the current-voltage conversion. We extract a range for the neck resistances of $\langle R \rangle = 100 \pm 35 M\Omega$. When a significant current is injected in a spine, the neck resistance can be inversely proportional to its radius, but not to the radius square, as predicted by Ohm's law. We conclude that the postsynaptic voltage cannot only be modulated by changing the number of receptors, but also by the spine geometry. Thus, spine morphology could be a key component in determining synaptic transduction and plasticity.

In Brief

Based on fluorescence recordings, Cartailler et al. recover the voltage dynamics in dendritic spines by deconvolution. They investigate electricity at a nanometric scale using electro-diffusion modeling and concluded that spine geometry and electrolyte shape the current-voltage conversion and electrical resistance.

*Correspondence: david.holcman@ens.fr.

[3]Lead Contact

SUPPLEMENTAL INFORMATION

Supplemental Information includes seven figures and can be found with this article online at https://doi.org/10.1016/j.neuron.2018.01.034.

AUTHOR CONTRIBUTIONS

T.K. and R.Y. elaborated and analyzed the experiments. D.H. and J.C. analyzed the data, developed the model and simulations, and wrote the manuscript.

DECLARATION OF INTERESTS

The authors declare no competing interests.

INTRODUCTION

Neurons communicate via synaptic microdomains, where an input current generates a voltage change in the post-synaptic neuron. This voltage change, induced by excitatory current, reflects the strength of the synaptic connection between two interacting neurons (Jack et al., 1975; Holmes et al., 1992; Koch and Segev, 1998, Chapter 2), (Qian and Sejnowski, 1989; Yuste, 2010) and depends on two components: the first is the number of glutamatergic receptors for excitatory neurons and the second is the geometry of the post-synaptic terminal. However the relative contribution between these two factors is still unclear. For example, the post-synaptic structure is often a dendritic spine, the geometry of which is involved in modulating the time-scale of diffusion (Svoboda et al., 1997; Korkotian et al., 2004; Bloodgood and Sabatini, 2005; Tønnesen et al., 2014; Holcman and Schuss, 2013). In parallel, increasing the number of receptors on that terminal leads to a larger synaptic current (Huganir and Nicoll, 2013; Elias and Nicoll, 2007; Kessels and Malinow, 2009). But diffusion alone is not sufficient to interpret the synaptic response because it is driven by electro-diffusion involving an electric field and diffusing ions. Electro-diffusion has been applied successfully for studying ionic fluxes and gating of voltage channels (McLaughlin and Poo, 1981; Bezanilla, 2008; Eisenberg, 2007). Those studies were all based on the fact that at the nanometer scale, the cylindrical symmetry of a channel model reduces to a one-dimensional segment, allowing the study of the electric field and charge densities in the channel pore (Eisenberg, 1999; Eisenberg et al., 1995). Moreover, recent studies have clearly shown that the current in the synaptic cleft reflects the coupling between moving ions and the local electrical field (Sylantyev et al., 2013; Savtchenko et al., 2004).

In a dendritic spine, voltage changes during the synaptic response are generated by the interactions between the ionic flow and the spine geometry. Dendritic spines are heterogenous microdomains at the limit of optical resolution and for that reason, voltage changes were estimated for many years using modeling and numerical simulations of passive cable equations, the basis for the Hodgkin-Huxley model (Koch and Segev, 1998). This approach is however not appropriate for spines because their micro-geometry composed of a bulby head connected to a thin neck is significantly different from that of a cable. In addition, cable theories break down when applied to small neuronal compartments, such as dendritic spines, because they assume spatial and ionic homogeneity. Linear approximations of electro-diffusion that couples the electric field with the ionic flow have been used to improve the estimation of the voltage changes in spines, approximated as cylinders of various sizes, but assuming local electroneutrality (Qian and Sejnowski, 1989). This method was later on generalized to study the electrical effect of Ranvier node (Lopreore et al., 2008). Recent advent in estimating the voltage changes at a sub-micrometer resolution (Araya et al., 2006, 2014; Hochbaum et al., 2014; Jayant et al., 2017) revealed electrical properties of dendritic spines (Harnett et al., 2012; Holcman and Yuste, 2015; Savtchenko et al., 2017), but the heterogeneity of the results (Popovic et al., 2015; Acker et al., 2016) and the absence of a robust computational framework and theory to interpret data challenges our understanding of electrical properties of these structures and cellular microdomains in general.

To better understand how spines function, we develop here an electro-diffusion framework to compute the voltage-current relation and the local voltage variations generated by synaptic inputs. We present a deconvolution procedure to recover the timescale of voltage responses from voltage-sensitive indicators in hippocampal neurons. Genetically encoded voltage indicators (GEVIs) (Brinks et al., 2015; Gong et al., 2015; Han et al., 2013; Jin et al., 2012; St-Pierre et al., 2014) can be expressed in neuronal membrane through plasmid transfection (Kwon et al., 2017) and thus it reports internal changes of the membrane voltage. The deconvolution procedure transforms the voltage dye Arclight response into voltage dynamics. To interpret the drop of voltage between the spine head and dendrite, we use the Poisson-Nernst-Planck theory for electro-diffusion. We further compute how a current flowing inside the spine head is converted into voltage and determine the electrical resistance. Numerical simulations of the voltage drop in the entire spine reveal how a change in the neck length and radius alters voltage. The manuscript is divided in two parts: first, we present the general method of time series deconvolution applied here to voltage dyes and we construct an electro-diffusion model to extract parameters from data. In the second part, we use our electro-diffusion model to generate three-dimensional simulations to investigate how the spine geometry modulates its electrical properties. We conclude here that while the numbers and the types of synaptic receptors determine the injected current, the geometry of a dendritic spine controls the conversion of current into voltage.

RESULTS

Converting Arclight Fluorescent Signals into Voltage Responses

Arclight dye indicators respond to voltage with an intrinsic delay (Kwon et al., 2017), such that a fast voltage response leads to a convolved fluorescence response. In that context, a synaptic input entering a dendritic spine generates a fluorescent response that needs to be deconvolved in order to recover the electrical genuine time course. As the voltage intensity has already been deconvolved in Kwon et al. (2017), we focus here on the temporal response. The basis of the method is to find the causal kernel $K(t)$, which is computed empirically by comparing the electro-physiology and the fluorescence responses in the soma (see STAR Methods). Once the kernel is found, we will use it to recover the noisy voltage dynamics in much smaller structures such as dendritic spines and portions of dendrites.

We apply the deconvolution procedure on the soma region (Figure 1A), which transforms the fluorescence dye signal (dashed green) into the voltage response (black) (Figure 1B; see STAR Methods and Figure S1). The deconvolved signal is shown by a line (green) that superimposes with the electrophysiological recordings (continuous black line). This result confirms the validity of the method. Indeed, by using the direct convolution of the electrophysiological recording by the kernel, we obtain the response (black curve) that exactly super-imposes with the fluorescence soma signal (Figure S1A). We note that the second bump in the fluorescence signal (dashed green) in Figure 1B is removed by the fitting procedure before the deconvolution kernel $K(t)$, as expected because the electrophysiological recordings do not exhibit this second bump. We extended the deconvolution procedure for several spikes in Figure S2.

Based on the deconvolution kernel $K(t)$, we shall now deconvolve the fluorescent responses in the regions of interest (ROIs) $R1$ and $R2$ shown in Figure 1C and Figure S3. Indeed, after we found the deconvolution kernel $K(t)$ from the soma data, we applied it to deconvolve the signal in spines because the distribution of dyes is the same in the entire neuron (Kwon et al., 2017). The results are shown in Figures 1D and 1E for the voltage in the spine head and dendrite. We note that the original fluorescence (thin line) contains fluctuations (Figures 1D and 1E) and an additional step is needed to remove the fluctuations (see STAR Methods and Figures S1C–S1E). We found that the voltage timescale in the dendritic spines, recovered from the present de-convolution procedure, is slower than the expected direct synaptic response. Probably, this slow timescale compared to direct synaptic electrical stimulation is due to glutamate uncaging, that can last for hundreds of milliseconds. To conclude, we can now recover the voltage in region $R1$, which represents the head, and in $R2$, which refers to the adjacent portion of the dendritic shaft at the base of the spine (Figure 1F). This deconvolution step is crucial because it allows us a direct comparison with the electro-diffusion model that we shall describe in the next section.

Electro-diffusion Theory for Ionic Flows in Dendritic Spines

To interpret the voltage dynamics in a dendritic spine, we use the electro-diffusion model that couples positive $c_p(x, t)$ and negative $c_m(x, t)$ charge concentrations with the electrical potential $V(x, t)$. The model is based on the phenomenological Poisson-Nernst-Planck (PNP) equations, where the ionic flow is driven by diffusion and the electric field. The voltage is described by the classical Poisson equation (Jackson, 2007, Sect.1.7) (see STAR Methods). We use the PNP equations to model the flow of ions when a current $I_{stim}(t)$, composed exclusively of positive charges, is injected at the top of a dendritic spine. We recall that the electrical potential generated by a flow of ions is defined up to an additive constant.

We start with the description of the voltage response produced by an input current $I(t)$ inside the spine neck. The current $I(t)$ that arrives at the neck entrance results from the stimulation current $I_{stim}(t)$ received by the head. We applied the electro-diffusion approach at the nano-micrometer scale, by reducing the neck geometry to a one-dimensional wire of length L (Figures 2A–2C). Due to its large size, compared to a dendritic spine, the dendrite constitutes an ionic reservoir (fixed concentrations).

Furthermore, using for the internal resistivity the value 109 $\Omega.cm$ (Koch, 2004, Chapter 11), we find that the fluctuations of the voltage in the portion of the dendrite $R2$ (Figure 1C) are negligible, and in that case, the region $R2$ is expected to be iso-potential. Consequently, we fix in the dendrite the value for the voltage $V(0, t) = 0$mV. We thus interpret the potential $V(t) = V(L, t)$ computed at the end of the neck (Figures 2A–2E) as the difference of potential between the entrance and the end of the spine neck. Consequently, we describe the electro-diffusion inside the neck by the ensemble of Equations 37, 39, and 40, where $I(t)$ has yet to be estimated.

From the classical theory of electricity (Jackson, 2007), it is not possible to extract the current passing through a passive device from the difference of potential when the resistance is unknown. However, using an electrical model for the axial current, escaping from the spine head to the neck, we shall reconstruct the voltage in the neck and recover the current in

the entire spine. Because there is no direct measurement of the current $I(t)$, we develop here a procedure (STAR Methods) to estimate this current from the measured membrane potential $\phi(t)$ in the spine head. We decompose the current as the sum of a resistive and a capacitive term:

$$I(t) = G\phi(t) + C\frac{d\phi(t)}{dt}. \quad \text{(Equation 1)}$$

The conductance G and the capacitance C reflect how the current $I_{stim}(t)$, injected in the spine, is processed by the head, depending on the intrinsic properties of the spine head (in the next section, we will simulate the entire voltage using PNP starting from the current entering through the channels). Consequently, we will refer to G and C as intrinsic conductance and intrinsic capacitance, respectively. We now estimate the two constants C and G and the voltage drop across a spine neck by solving numerically Equations 37, 39, and 40 and compare the results to the simulations with the deconvolved Arclight fluorescent voltage response. The response is generated following glutamate uncaging stimulations at the top of the spine head (Figure 1C, red dot). We solve numerically the PNP equations for the distribution of positive $c_p(x, t)$ and negative $c_m(x, t)$ charges, as well as the potential difference $V(x, t)$ (Figures 2D and 2E). To estimate the voltage difference $\Delta\tilde{V}(t)$ across the neck, we grounded the potential to 0 mV at the dendritic shaft (before stimulations, the voltage is described by Equation 38).

To assess whether the potential difference $\Delta\tilde{V}(t) = V_{head}(t) - V_{dend}(t)$ can be predicted from the electro-diffusion model, we fix the input voltage $\phi(t) = V_{head}(t)$. We then compare the voltage obtained by solving Equations 37, 39, and 40 (Figures 2D and 2E) to the measured voltage $V_{dend}(t)$ in region $R2$ (blue) at the dendritic shaft (Figure 2C). Although region $R1$ includes the head and the neck, we neglected the fluorescence in the neck due to its small thinness $\leq 100nm$. We found a good agreement between the experimental data and numerical simulations (Figure 2D) showing that the difference of voltages between the head and dendrite can be predicted from the input voltage $V_{head}(t)$. In addition, we estimated the injected current (Figure 2E, see STAR Methods and Equation 1) directly without any direct electrophysiological recordings. Note that the deconvolved voltage in the head (blue) and the computed current (red) are exactly proportional, because the capacitance C, reported in Table 1 and used to compute $I(t)$ in Equation 1, is negligible. Thus, the current is simply proportional to the voltage. We conclude at this stage that the electro-diffusion theory allows estimating the electrical properties of the spine red neck and the injected current (of the order of tens of pA) in the spine neck, triggered by a synaptic current $I_{stim}(t)$.

We apply systematically the electro-diffusion approach, based on (1), to extract the capacitance C and the conductance G of several spines (Figures S3 and S4). Using an optimization procedure, we explore the parameter space for computing C and G (Figure S4). We minimize the error between the solution of the electro-diffusion equation and the voltage output of the dendrite during a small time interval at the beginning of the response (Figure S4). The resistance is computed by averaging the voltage changes in time. We use for the estimator the expression $R_{neck} = \langle V(0, t) - V(L, t)\rangle / \langle I(t)\rangle$ (where the average is performed

over the time interval $t \in [0, 0.4]s$). In all cases, we find a good agreement (Figure 4) between the measured and computed voltage drop across the spine neck, where we estimated the current injected in the neck from the head of several spines.

In summary, we found that the average spine neck resistance (for a mean neck radius $r_o = 100nm$) is $\langle R \rangle \approx 100 \pm 35M\Omega$ (Table 1). We also reported here a large variability in the spine resistance, while the intrinsic capacitance is negligible. To conclude, the electro-diffusion model allows computing the current injected in the spine neck after a synaptic stimulation, thus recovering the neck resistance.

Voltage Transduction in a Spine and Predictions of Electro-diffusion

We have shown in the previous section that electro-diffusion PNP-based model can be used to analyze Arclight fluorescence recording and this model allows estimating the current flowing in the spine neck. We shall now extend the PNP model to geometries that characterize the peculiar shape of the dendritic spines. To analyze how a dendritic spine influences the voltage response to a synaptic input, we simulate the three-dimensional PNP equations (see STAR Methods) for two geometries: a ball of radius r_{head} and a spine-like geometry (Figure 3). We computed the distribution of the electrical potential for short spine necks (Figure 3A), where the head contains two narrow openings: one of radius $r_o = 100nm$ representing the junction with the neck, and the other of radius $r_i = 10nm$ that receives the steady current I_{stim} of positive charges (Figure 3B). Note that we have dropped the time t in the expression of the current I_{stim}, since we consider now steady-state current. In addition we neglected the membrane capacitance because the current I_{stim} represents already the ionic flow entering the head. We show (Figure S5) that the capacitance has almost no contribution to the voltage drop. We computed the distribution of positive $c_p(\boldsymbol{x})$ and negative $c_m(\boldsymbol{x})$ charge concentrations as well as the voltage $V(\boldsymbol{x})$ when it is grounded to 0 V at the end of the spine neck, which represents the connection to the dendrite, considered as a large ionic reservoir with fixed concentration (see Table 2). Consequently, $V(\boldsymbol{x})$ represents the voltage difference induced by the injected current I_{stim}. We find the distribution of the voltage along the x axis (blue) Figure 3B when $I_{stim} = 150pA$ is injected in the spherical geometry as shown in Figures 3A and 3B.

In summary, inside a spherical domain, diffusion is the dominant driving force and the potential drop is reduced significantly, which is equivalent of having a small spine head resistance. Indeed, applying the electro-diffusion model (Equations 37 and 38) to a spine-like geometry (Figure 3C), we observe that most of the voltage drop is carried by the spine neck (Figure 3D). Interestingly, it is not equivalent to decrease the neck length to compensate for a decrease in the injected current (see result with an injected current of 150 versus $300pA$), suggesting that changing the synaptic weight by adding or removing receptors or modifying spine neck length have different consequences on the spine voltage distribution.

We also observed in Figures 3E–3G that there is a narrow layer located at the entrance of the PSD region where the synaptic current I_{stim} is injected. We found a 7 mV drop occurring in a small distance ($\approx 50nm$) inside the spine head. This small region of large convection is at the limit of actual resolution ($\approx 0.116\mu m$/pixel). We could thus define a boundary layer

resistance R_{bl}. Outside this layer, the voltage is quite uniform, leading to a reduced field convection $e/k_BT\nabla\phi$ (Equation 37), demonstrating that diffusion is dominant inside the spine head. To conclude, we demonstrated numerically using PNP equations that the voltage drop in the spine head is negligible (less than a quarter of mV), except in a small region where the current is injected. These results are in contrast with the classical cable theory (Figure S6), which suggests that the motion of ions is driven by the voltage gradient. At this stage, electro-diffusion theory predicts that the voltage in the spine head $V_{head}(t)$ is spatially homogeneous, confirming the approximation of Equation 1, except near the post-synaptic density or at the entrance of the spine neck. The global spine head resistance is thus negligible, since the potential drop occurs just at the end of the neck, and thus the entire spine resistance is carried by the neck and the boundary layer: $R_{spine} \approx R_{neck} + R_{bl}$. Note that in practice the resistance R_{bl} is not accessible to experimental measurements due to the thin region where it is generated. Thus, experimental results give access values for the neck resistance R_{neck}.

Spine Geometry Determines the I–V Conversion

To study the influence of the geometrical parameters on the electrical property of a spine, we first estimated the effect of the spine head radius r_{head} for five spines (Figure S3). By measuring their projected area S_{head} from the two-photon images, we use relation (Figure 4A)

$$r_{head} = \sqrt{\frac{S_{head}}{\pi}} \quad \text{(Equation 2)}$$

to extract the equivalent radius (blue stars). We then use the PNP model associated to the short spine with no neck (Figure 3A) to estimate the average voltage difference $\langle V \rangle_{ball}$ (for a current of $100pA$) between the north and the south pole of a spine head. We find that the mean voltage varies in a range of $1.5 - 1.6mV$, when the radius of the head varies in the range $0.3 - 1.5\mu m$. This result shows that the head radius had little influence on the mean voltage.

We then estimated how the spine neck resistance R_{neck} depends on the neck length and width, usually unaccessible using classical microscopy approaches: we find both theoretically and experimentally that the resistance increases (blue stars) with the neck length L (Figures 4B, 2D, and 2E). Note that the size of the head is not correlated with the resistance (Table 1). Furthermore, electro-diffusion simulations in a segment using (37–38) predicts that for the mean current input extracted from data, there is a significant change in the local concentration of positive charges (simulations of the 1D neck) of length $L = 0.7\mu m$ at the time-to-peak ($t_0 = 55ms$). Indeed, we find a concentration gradient of $33mM$ between the tip and the base of the neck, when the concentration of ions is fixed at 163 mM in the dendrite (Figures 4C and 4D). Although the injected current $I(t)$ is composed of positive charges, the concentration gradient in the neck is driven by positive and negative charges. Such phenomenon is called concentration polarization (Strathmann, 2004, Chapter 4). Finally, we confirmed this result using a simulation in a three-dimensional spine (neck plus

head), where we injected transiently a current with an amplitude $I_{stim} = 150pA$ (resp. $I_{stim} = 150pA$) at the top of a spine domain (Figure S6) and found a concentration gradient of $22mM$ (resp. $45mM$) in the neck.

Finally, using the electro-diffusion theory and the spine parameter $r_{head} = 0.5\mu m$, $L = 1\mu m$, we estimated the I–V relation for various neck radius, showing a saturation for large current (Figure 4E). These curves show that the neck radius is one of the most critical parameters in defining the conversion of current into voltage. Then to clarify the dependency of the spine neck resistance R_{neck} on its radius, we simulated the PNP equations by solving Equation 58, where a steady-state current $I_{stim} = 20; 50; 100; 150pA$ is injected inside the spine head (Figure 3C). We obtained the average voltage inside the head $\langle V \rangle_{head}$. We plotted the resistance of the neck versus the neck radius r_0, computed by $R_{neck} = \langle V \rangle_{head}/I_{stim}$ in Figure 4F. Interestingly, we find that depending on the injected current, the spine resistance can decay inversely proportional to the radius of the neck. This is in contrast with classical results based on electrical circuit approximation (Koch, 2004, Chapter 12), where the classical Ohm's law for a resistance predicts that resistance depends on $1/r_0^2$. When the injected current is large $I_{stim} = 150pA$, the resistance seems to decay with a power law $1/r_0$ (dotted red) but changes to $1/r_0^{3/2}$ (dotted blue) for $I_{stim} = 20pA$. We recover the classical law for a small current $I_{stim} = 1pA$. Finally, for $I_{stim} = 50pA$ and a spine neck radius of $r_0 = 50nm$ (resp. 100 nm), the overall spine resistance that is mostly carried by the neck would be $R_{spine} \approx R_{neck} = 120M\Omega$. These results show a clear deviation from the classical Ohm's law and also a limitation of the diffusion approach (Svoboda et al., 1997).

In summary, we used the electro-diffusion theory and the Arc-light fluorescent data to characterize the electrical properties of a dendritic spine. With respect to a synaptic input, a spine can be electrically characterized as a diode device (Figures 5A and 5B) with a finite resistance (for a small current), saturating for large currents (Figure 5C). The voltage difference varies from few to tens of mV. However, from the perspective of a Back Propagation Action potential, the equivalent circuit of a spine is a diode with zero resistance (no leak current; Horowitz and Hill, 1989, Chapter 1; Figure 5D).

DISCUSSION

We developed here a computational approach based on the electro-diffusion theory to estimate the electrical properties of dendritic spines. We first deconvolved the Arclight fluorescent signal and then applied the electro-diffusion theory to estimate the resistance and the capacitance from hippocampal neuron data. Our approach contrasts with classical estimation of the spine neck resistance and dendritic spine electric properties, extracted in the context of the electrical circuit approximation, passive cable theory and even diffusion approximation (Svoboda et al., 1997; Popovic et al., 2015; Acker et al., 2016; Koch, 2004, Chapter 2). In contrast to those studies, we find here that the electro-diffusion coupling is the main driving force for ionic current in the spine neck (Figure 3), while diffusion is sufficient to describe the motion of ions inside the head. The electric field is negligible in the head, except very close to the entrance of the synaptic input and at the exit with the neck.

In fact, electro-diffusion theory reveals that the spine head geometry imposes that the voltage is almost constant in the head, while the neck is responsible for most of the voltage drop. This is in contrast with the predictions of the cable theory or previous approximations of electro-diffusion (Koch and Segev, 1998), based on electroneutrality and no gradient of charges. We also demonstrated here that the ion conduction is mostly driven by diffusion in the spine head, suggesting that the head resistance is negligible compared to the neck.

We showed here that the synaptic current leads to a gradient of concentrations and thus the Poisson-Nernst-Planck theory should be used to describe the voltage at the submicron level. We presented in Figure 3 a resistance R_{bl} in a small boundary layer associated to a drop of voltage. This model may suggest that scaffolding proteins and receptors located in the PSD are experiencing large voltage drop that could regulate the electrical properties of charged C terminus of the receptors such as AMPA and thus their trafficking in dendritic spines (Nicoll, 2017; Herring and Nicoll, 2016). For slower electrical events, ionic concentrations should follow the changes of the local voltage and there is a significant gradient of charges of the order of 150 mM in a spatial scale of 1 μm, although the average concentration is stable around 100 mM. However, this effect does persist for a transient current lasting 100 ms, where the concentration gradient at time to peak is of the order of 30 mM. Most likely, fast oscillations or voltage fluctuations due to the opening and closing of the channels will not lead to an extended concentration gradient and, in that case, the electro-diffusion could be neglected.

It remains difficult to study the exact local balance of positive by negative charges, because in transient regimes or at equilibrium, positive charges are all the time in excess. Possibly the sum of negatively ionic charges plus the negative charges located on immobile proteins can balance positive charges at a tens to hundreds of nanometers. Long-range electro-diffusion effects have already been described for directing the current flow in the synaptic cleft into the post-synaptic terminal (Sylantyev et al., 2008, 2013), showing in a different context that electro-diffusion drives ionic flows and the voltage in neuronal microdomains.

Time Deconvolution of the Arclight Fluorescent Signal

Neuronal voltage is reported by recording electrodes and we showed here how the Arclight signal can be deconvolved in small and large microdomains, so that we can now access the voltage dynamics and electrical properties from microdomains. Genetically encoded activity sensors combined with microscopies are now classically used (Emiliani et al., 2015) to record and manipulate the activity of neural circuits. We show here how fluctuations contained in the fluorescent signal can be filtered and the voltage time course is recovered from the empirical kernel $K(t)$ (STAR Methods). This approach can be applied to any encoded activity sensor expressed in neurons and only requires the comparison of the electrophysiological recording with the florescence in the soma. The present deconvolution could also be used to recover the electrical activity from slow calcium indicators (Emiliani et al., 2015).

Influence of the Neck Radius on the Spine Resistance

The spine neck radius cannot be spatially resolved, so any geometrical fluctuation is likely to result in a drastic change in the resistance. For diffusion alone, the rate of extrusion (Holcman and Schuss, 2013) (for Brownian particle) from a dendritic spine is given in first approximation as $(|\Omega_{spine}|L/D\pi r_o^2) + (C_2|\Omega_{head}|R_c^{3/2}/Dr_o^{3/2})$, where D is the diffusion coefficient, $|\Omega_{spine}|$ is the volume of the spine, L the length of the neck, R_c the radius of curvature at the base of the neck-head junction, $|\Omega_{head}|$ the volume of the head and C_2 a constants, and r_o is the radius of the neck. This expression shows that a small change in the radius r_o (dividing by two for example) leads to a significant change of at least 4 for the diffusion time-scale. We addressed the radius neck uncertainty here in the context of electro-diffusion by computing the neck resistance for different radii (Figure 4F).

Spine-intrinsic electrical characteristics are revealed by the impedance, which is the ratio of the voltage to the injected current. For example, for a steady-state current of $I = 50pA$, the Ohmic resistance of a spine of radius $100nm$ (resp. $50nm$) is $\langle R_{neck}\rangle = 120M\Omega$, (resp. $\langle R_{neck}\rangle = 350M\Omega$). This high resistance value for longer spine necks could be relevant for the statistics collected in brain slices (see our computations for the spine neck resistance in Figures S7D and S7E, where we find that the key parameter remains the spine neck radius; confirmed in Beaulieu-Laroche and Harnett, 2018). However, there is still no consensus about the large range of spine resistances, reported in the literature with direct and indirect measurements: the conclusions of different optical studies are mixed: some suggest an attenuation of EPSPs (Araya et al., 2006, 2014; Harnett et al., 2012), other suggest instead that spines are isopotential with the dendrites and do not alter EPSPs (Svoboda et al., 1997; Tønnesen et al., 2014). Diffusional studies of small fluorescent molecules through spines have predicted neck resistances of $4 – 50M\Omega$ (fluorescein dextran) or $56M\Omega$ (Alexa Fluor 488), (Svoboda et al., 1997; Tønnesen et al., 2014). Other studies suggested a lack of voltage filtering of dendritic spines during glutamate uncaging (Popovic et al., 2015; Acker et al., 2016) with a resistance of $30M\Omega$. We find here for the neck resistances a range of $[100 – 300]M\Omega$, compared to $13 – 297M\Omega$, reported in Kwon et al. (2017). However, this large range of values may reflect the heterogeneous distribution of neck radii and in particular the smallest constriction along the neck. The decay of the EPSPs from the spine head to the parent dendrites can be explained by the law of electro-diffusion in the spine geometry. We have shown here that the electrical compartmentalization is mostly due to the resistance of the neck.

Interestingly, we also found here that the resistance of a dendritic spine is inversely proportional to the radius of the neck r_0, and not by the square r_0^2, as classically described for electrical devices (Figure S6) (Svoboda et al., 1997). This result shows that the neck size has a key effect in modulating the spine electrical resistance. Another prediction of the present theory is that a synaptic current injected in a spine head should be of the order of $100pA$ (as suggested in Figure 2E). The shortest diameter of a spine neck along its length is certainly a key factor that could drastically affect its resistance. Indeed, the critical geometrical parameter is the minimal shortest constriction along the neck (Holcman and Schuss, 2013),

which could further be influenced by the crowding due to the internal endoplasmic reticulum (Holcman and Yuste, 2015).

The Geometry of Dendritic Spines Modulate the Voltage Changes Independently of the Input Current

Dendritic spines are involved in modulating two- and three-dimensional receptor trafficking (Huganir and Nicoll, 2013; Elias and Nicoll, 2007; Kessels and Malinow, 2009), molecular post-synaptic density composition, calcium diffusion (Yuste, 2010; Korkotian et al., 2004), synaptic transmission, and plasticity. We have shown here using the electro-diffusion framework that the voltage in dendritic spines can also be controlled by changing the neck length geometry. This modulation obtained by changing the geometry is complementary to the possible changes in the number of receptors, resulting in a long-term modification of the synaptic current, reflecting synaptic plasticity.

Changing the spine neck length can thus regulate the local dendritic voltage that contributes to the genesis of an action potential. We further confirm previous experimental findings in brain slices (Araya et al., 2006, 2014), showing that the synaptic voltage amplitude is inversely correlated with the neck length, but we found here a much stronger effect compared to previously evaluated (Popovic et al., 2015). However, in agreement with Popovic et al. (2015), we do not need to use any additional active channels in the electro-diffusion model to account for the voltage in the spine, suggesting that they might not play a predominant role.

To conclude, voltage changes in dendrites can now be detected at the nanometer scale and the electro-diffusion theory allows interpreting these data and predicts a nonlinear current-voltage relation imposed by the specific geometry of dendritic spines. While the spine geometry controls voltage, the synaptic current is set by the number of receptors (Huganir and Nicoll, 2013; Elias and Nicoll, 2007; Kessels and Malinow, 2009). These two mechanisms are supposed to be independent and they are both involved in controlling the synaptic response. It would certainly be interesting to study how changes in one affect the other.

Finally, spine twitching (hypothesized in Crick, 1982 and demonstrated experimentally in Korkotian and Segal, 2001a, 2001b) may impact the electrical property of spines. Indeed, the consequence of the spine head constriction might be negligible for the voltage inside the head but could influence the current inside the neck and thus reduces the effective resistance.

STAR ★ METHODS

Detailed methods are provided in the online version of this paper and include the following:

KEY RESOURCES TABLE

REAGENT or RESOURCE	SOURCE	IDENTIFIER
Deposited Data		

REAGENT or RESOURCE	SOURCE	IDENTIFIER
Fluorescence data	Kwon et al., 2017	N/A
Software and Algorithms		
MATLAB 2015	MathWorks	https://fr.mathworks.com/; RRID: SCR_001622
COMSOL Multiphysics	COMSOL	https://www.comsol.com/; RRID: SCR_014767
Deconvolution algorithm	This paper	N/A

CONTACT FOR REAGENT AND RESOURCE SHARING

Further information and requests for resources and reagents should be directed to and will be fulfilled by the Lead Contact, David Holcman (david.holcman@ens.fr).

METHOD DETAILS

Arclight signal—We briefly described here the experimental data we have used for our electro-diffusion theory and time deconvolution. There are fully described in (Kwon et al., 2017). The protein-based voltage indicator ArcLight is injected in primary cultured hippocampal neurons. ArcLight expressing dissociated hippocampal culture neurons in DIV 12–16 were recorded in artificial cerebrospinal fluid (ACSF) containing ions of various concentration. Two-photon glutamate uncaging was done with a custom-made two-photon laser scanning microscope. In glutamate uncaging, the location of stimulation was selected with 1–2 μm distance from dendritic spines, not closer than 1μm. The whole-cell patch clamp and the glutamate uncaging were performing while doing the wide-field one photon imaging of ArcLight fluorescence. Finally, we used the voltage deconvolved from the fluorescence signal, based on a two-state model of voltage dependent ArcLight fluorescence described in (Kwon et al., 2017).

Distribution of the arclight genetically encoded voltage indicator—We used here the genetically encoded voltage indicators (GEVIs) (Brinks et al., 2015; Gong et al., 2015; Han et al., 2013; Jin et al., 2012; St-Pierre et al., 2014), which can be expressed in neuronal membrane through plasmid transfection. This dye is used for an optical measurements of the membrane potential. ArcLight was expressed in cultured mouse hippocampal neurons and the fluorescence was imaged with an upright fluorescence microscope and a fast sCMOS camera. To monitor somatic electrophysiology, imaged neurons also were patched in whole-cell, current clamp mode. In neurons expressing ArcLight, fluorescent signals were clearly visualized in dendritic spines as well as soma.

To test how the ArcLight fluorescence responsed to bAPs generated by somatic current injection, the eletrophysiological signals were recorded from areas of interest (ROI) in somata, proximal dendrites and spines. To quantify optical signals, we measured the relative change in fluorescence intensity $-\Delta F/F$, a quantity directly proportional to membrane potential (Peterka et al., 2011).

Intracellular ArcLight proteins located in ER and Golgi may contaminate baseline fluorescence (F) because they are fluorescent, but insensitive to membrane potential, as they

are too far from the Debye length of the membrane's electric field. Although ArcLight is in a dark state at the lower pH of intracellular organelles (Han et al., 2014), its contribution to background could be critical to determine $-\Delta F/F$, if averaged together with a membrane responding ArcLight. To evaluate this possibility, it was calculated (Kwon et al., 2017) the activity probability of each pixel in response to voltage by using a constrained non-negative matrix factorization (CNMF) algorithm (Pnevmatikakis et al., 2016) and compared the resulted weight matrix image to the base fluorescence image. Through this comparison, we identified regions of non-responding intracellular ArcLight in the soma, which has strong base fluorescence yet low activity weight, while there were no such regions in dendrites and spines. This result implies that the trafficking mechanism of ArcLight proteins is by ER translation at inactive sites of soma, and then targeting to adjacent somatic cell membrane and by diffusion to the rest of the cell along the cell membrane. In summary, the Arclight dye is inserted in the membrane where the voltage sensor is located in the cytoplasm and thus it reports internal changes of the membrane, that we analyze here.

We also recall that spines are potentially electrotonically (Kwon et al., 2017) far from the soma and experiments with CsCl-based internal solution to block leak K+ channels make the neuron electronically compact. The average amplitude of bAP in spines was indistinguishable from that of parent dendrites (Kwon et al., 2017). Voltage step depolarizations in voltage clamp show that the measured somatic voltage was same as the optically measured voltages of spines and dendrites. Somatic voltage before background noise subtraction were larger than voltages of spines and dendrites because of the closer proximity to the brighter somatic region. These results confirm that the voltage dyes in the spines and dendrites are reliable reporters of the voltage and thus no further recalibration is necessary to analyze the fluorescent in the spine compared to the soma.

Deconvolution Kernel—To recover the intrinsic voltage dynamics $h(t)$ from the slow Arclight signal $A_{rc}(t)$, we compare the electrophysiological patch-clamp recording in the soma with the ArcLight fluorescence extracted from the somatic region delimited in the image (Figure 1A). This comparison is at the basis of the deconvolution method of the causal fluorescent signal. Indeed, the slow Arclight reporter convolves the fast electrical voltage signal, modeled by a kernel function $K(t)$ with the intrinsic dye dynamics, leading to a slow fluorescent response. The kernel $K(t)$ describes the time delay of the fluorescence activation compared to the voltage dynamics. We model the kernel by the function

$$K(t) = \frac{A}{\tau^2} t e^{-\frac{t}{\tau}}, \quad \text{(Equation 3)}$$

where the value of the parameters A and τ are obtained by comparing the Arclight response in the soma with the convolution of the electrophysiological recordings (Figure S1). Indeed, for a voltage signal $h(t)$, the Arclight signal $A_{rc}(t)$ is expressed by the convolution product

$$A_{rc}(t) = \int_0^t K(t-s)h(s)ds \quad \text{(Equation 4)}$$

To recovered $h(t)$ from the Arclight signal $A_{rc}(t)$, we first calibrated the kernel $K(t)$ so that the Arclight signal peaks exactly at the one monitored by the electrophysiological signal (Figure 1B) and we obtain $\tau = .05s$. The other parameter A is a scaling that will be adjusted for each experimental data. The kernel $K(t)$ is plotted in Figure S1B.

Noise filtering and approximation—In small dendrite and dendritic spine regions, the Arclight data contains a large noise that should be removed. For that purpose, we use a Savitzky-Golay filter (Savitzky and Golay, 1964), to increase the signal-to-noise ratio. We shall now describe how we have removed the high frequency fluctuations present in the fluorescence signal (Figure S1C). We use the Savitsky-Golay (SG) filter, which is based on local least-squares polynomial approximation. The filter reduces the fluctuations while maintaining the shape and height of the initial signal (Savitzky and Golay, 1964).

Savitsky-Golay filter—The Savitsky-Golay filter is based on decomposing the input fluorescent signal A_{rc} that we now denote by F into polynomials. We start with the sampling,

$$F(t) = \sum_{k=1}^{N} F(t_k)\delta(t-t_k), \quad \text{(Equation 5)}$$

where N is the number of points. We define the discrete time subinterval $I_k = \{t_k - n\Delta t \cdots, t_k \cdots t_k + n\Delta t\}$ of size $2n+1$ time points, separated by a time step Δt. The filter is constructed by finding an ensemble of polynomials iteratively on each time window I_k. We define the sequences F_q of functions $q = 0..N$, where $F_0 = F$. To compute the polynomial of degree p,

$$P_k(t) = \sum_{i=0}^{p} a_{k,i} t^i, t \in I_k \quad \text{(Equation 6)}$$

that approximate the function F, we start with $k = 1$: the coefficients $a_{1,i}$ are computed by minimizing on the interval I_1

$$\min_{t \in I_1} R_1^2(t), \quad \text{(Equation 7)}$$

where

$$R_1^2(t) = \sum_{s=0}^{n} \left(F_0(t_1 + s\Delta t) - P_1(t_1 + s\Delta t)\right)^2 . \quad \text{(Equation 8)}$$

The function F_1 is constructed from F, by replacing $F(t_1)$ by $P_1(t_1)$,

$$F_1(t) = \{P_1(t_1), F(t_2), \cdots, F(t_N)\} . \quad \text{(Equation 9)}$$

In general, the k^{th} – iteration is obtained by minimizing on I_k,

$$\min_{t \in I_k} R_k^2(t), \quad \text{(Equation 10)}$$

where

$$R_k^2(t) = \min_{t_k + s\Delta t \in I_k} \sum_{s=-n}^{n} \left(F_{k-1}(t_k + s\Delta t) - P_k(t_k + s\Delta t)\right)^2 . \quad \text{(Equation 11)}$$

The filtered function F_k at the k^{th} – iteration is given by

$$F_k(t) = \{P_1(t_1), \cdots, P_k(t_k), F(t_{k+1}), \cdots, F(t_N)\} . \quad \text{(Equation 12)}$$

The coefficients $\{a_{k,i}\}$, for $i = 0..p$ are obtained by differentiating R_k^2 (Equation 10) with respect to the coefficients $a_{k,i}$,

$$\begin{cases} \dfrac{\partial R_k^2}{\partial a_{k,0}} = 0 \\ \quad \vdots \\ \dfrac{\partial R_k^2}{\partial a_{k,p}} = 0. \end{cases} \quad \text{(Equation 13)}$$

The system of Equation 13 is a linear matrix equation,

$$\begin{bmatrix} F_{k-1}(t_k - n\Delta t) \\ \vdots \\ F_{k-1}(t_k + n\Delta t) \end{bmatrix} = \mathbf{V} \begin{bmatrix} a_{k,0} \\ \vdots \\ a_{k,p} \end{bmatrix}, \quad \text{(Equation 14)}$$

where $\mathbf{V}$ is the $(2n + 1, p + 1)$ matrix

$$\mathbf{V} = \begin{pmatrix} 1 & t_k - n\Delta t & (t_k - n\Delta t)^2 & \cdots & (t_k - n\Delta t)^p \\ 1 & t_k - (n-1)\Delta t & (t_k - (n-1)\Delta t)^2 & \cdots & (t_k - (n-1)\Delta t)^p \\ \vdots & \vdots & \vdots & \ddots & \vdots \\ 1 & t_k + n\Delta t & (t_k + n\Delta t)^2 & \cdots & (t_k + n\Delta t)^p \end{pmatrix}. \quad \text{(Equation 15)}$$

This matrix is inverted numerically in MATLAB. To conclude, the filtering procedure is summarized by

$$\mathcal{S}_G(F(t)) = \sum_{k=1}^{N} P_k(t_k)\delta(t - t_k). \quad \text{(Equation 16)}$$

We can iterate N_{SG} times the SG filter,

$$f(t) = (\mathcal{S}_G)^{N_{SG}}(F(t)), \quad \text{(Equation 17)}$$

where $(S_G)^{N_{SG}} = S_G \circ \ldots \circ S_G$, N_{SG} times.

Preliminary treatment before using the Savitsky-Golay filter—We now segment the fluorescence signal: the first time interval starts at $t_{unc} = 0$ which is the initiation of the voltage response until the maximal response at time t_{peak} (see Figure S1C). Because the physical modeling of the dye kinetics (Kwon et al., 2017) predict a single exponential decay, we shall treat, after the time t_{peak}, any fluctuations as noise and we will apply the iteratively the SG filter (17). In summary, we divide the fluorescent response $F(t)$ into three subregions Figure S1C:

1. before the time of glutamate uncaging t_{unc},
2. from the time t_{unc} to the time-to-peak t_{peak},
3. after the time-to-peak t_{peak}.

In region 1 (before t_{unc}), we use the following parameters: polynomial degree $p = 2$, the size of the window $|I_k| = 40$ points and the number of iteration of the filter $N_{SG} = 1$ to 3

(depending on the signal). This filtering reduces the noise amplitude in this first region by 80%. The filtered signal is f_1. In regions 2 and 3, to preserve the signal peak amplitude, we use a hight degree polynomial and the parameters $p \geq 25$, $|I_k| = 100$, and $N_{SG} = 6 \pm 2$ to remove small fluctuations (Figure S1C). However, we note that the second bump of smaller amplitude around $t = 0.65s$ in Figure S1C is generated by the random fluctuations of the fluorescence signal. Nevertheless, these fluctuations do not impact our analysis because we use for our computations the time interval: $[0, 0.4]s$. In region 3, we remove large fluctuations using parameters $p \geq 5$, $|I_k| = 80$, and $N_{SG} = 5$. The filtered signals in regions 2 and 3 are f_2 and f_3 respectively.

To glue continuously the results on each region, we use the sigmoid function,

$$\sigma(t, t_{cut}) = \frac{1 + \tanh(\zeta(t - t_{cut}))}{2}, \quad \text{(Equation 18)}$$

where $\zeta = 150s^{-1}$ and t_{cut} is a parameter. Finally, from the input $A_{rc}(t)$, we obtain the filtered signal

$$f(t) = \sigma(t, t_{unc})(f_2(t) + f_3(t) - f_1(t)) + \sigma(t, t_{peak})(f_3(t) - f_1(t) - f_2(t)) + 2f_1(t) + f_2(t),$$

(Equation 19)

shown in Figure S1C.

Analytical approximation of the filtered signal and time deconvolution—We now described in detail the analytical approximation of the filtered signal f (previous section). The goal of this approximation is to remove any fluctuations that could be amplified in the deconvolution procedure. First, we project the filtered signal f on the two functions

$$f_{\alpha,\beta_1,\beta_2,\gamma_1,\gamma_2}(t) = t^{\alpha}(\beta_1 \exp(-\gamma_1 t) + \beta_2 \exp(-\gamma_2 t)) \quad \text{(Equation 20)}$$

where the parameters α, β_1, β_2, γ_1, γ_2 are obtained by the MATLAB optimization procedure polyfit (Figure S1D). This step eliminates any small fluctuations that could have been amplified in the deconvolution step (Figure S1E). Another advantage of having an analytical representation is to obtain an explicit Laplace's transformation used in the deconvolution. Indeed,

$$\hat{f}_{\alpha,\beta_1,\beta_2,\gamma_1,\gamma_2}(s) = \Gamma(\alpha+1)\left(\frac{\beta_1}{(s+\gamma_1)^{\alpha+1}} + \frac{\beta_2}{(s+\gamma_2)^{\alpha+1}}\right), \quad \text{(Equation 21)}$$

where $\Gamma(\cdot)$ is the Gamma function (Abramowitz and Stegun, 1966, Chapter 6). We now use the exact form of the kernel to obtain an explicit formula for the deconvolution. We recall that the convolution kernel is given by

$$K(t) = \frac{A}{\tau^2} t \exp\left(-\frac{t}{\tau}\right) \quad \text{(Equation 22)}$$

and its Laplace's transform is

$$\hat{K}(s) = \frac{A}{(s\tau+1)^2}. \quad \text{(Equation 23)}$$

The convolution product

$$f_{\alpha,\beta_1,\beta_2,\gamma_1,\gamma_2}(t) = (K * h)(t) \quad \text{(Equation 24)}$$

can be written in the Laplace's variable s

$$\hat{f}_{\alpha,\beta_1,\beta_2,\gamma_1,\gamma_2}(s) = \hat{K}(s)\hat{h}(s). \quad \text{(Equation 25)}$$

Thus using expression 23 and 21, we obtain

$$\hat{h}(s) = \frac{\hat{f}_{\alpha,\beta_1,\beta_2,\gamma_1,\gamma_2}(s)}{\hat{K}(s)} = \frac{\Gamma(\alpha+1)(s\tau+1)^2}{A}\left(\frac{\beta_1}{(s+\gamma_1)^{\alpha+1}} + \frac{\beta_2}{(s+\gamma_2)^{\alpha+1}}\right). \quad \text{(Equation 26)}$$

We can now compute h using the analytical result for the inverse Laplace of function

$$M(s) = \frac{C(s\tau+1)^2}{(s+\gamma)^{\alpha+1}} \quad \text{(Equation 27)}$$

with $a \geq 2$ and $0 \leq \gamma$ which is given by

$$m(t) = \frac{Ce^{-\gamma t}t^{\alpha-1}}{\Gamma(\alpha+1)}(t(1-2\tau\gamma)+2\tau\alpha) + \frac{C\tau^2 e^{-\gamma t}t^{\alpha-2}}{\Gamma(\alpha+1)}\left((t\gamma)^2+\alpha^2-\alpha-2\gamma\alpha t\right). \quad \text{(Equation 28)}$$

Finally, we obtain the expression for the deconvolved voltage signal

$$h(t) = \frac{\beta_1 e^{-\gamma_1 t}}{A}\left(t^{\alpha-1}(t(1-2\tau\gamma_1)+2\tau\alpha) + \tau^2 t^{\alpha-2}\left((t\gamma_1)^2+\alpha^2-\alpha-2\gamma_1\alpha t\right)\right) + \frac{\beta_2 e^{-\gamma_2 t}}{A}$$

$$\left(t^{\alpha-1}(t(1-2\tau\gamma_2)+2\tau\alpha) + \tau^2 t^{\alpha-2}\left((t\gamma_2)^2+\alpha^2-\alpha-2\gamma_2\alpha t\right)\right).$$

(Equation 29)

To conclude, we obtain here the expression for the deconvolution of (29) from the analytical approximation of the Arclight fluorescent signal A_{rc}, described in Figure S1E. Note that the value of the parameter A is calibrated for each dataset, such that the maximum amplitude between the Arclight response and the deconvolved voltage remains identical.

Deconvolution method applied on several peaks—The deconvolution procedure described in the above section can be extended to signals with several peaks. To illustrate the result of the deconvolution method, we use an input made of two consecutive spikes (Figure S2A), generated for example from a post-synaptic voltage response (Tsodyks and Markram, 1997). The two spikes are shown in Figure S2B (dashed black). We now summarize the steps of this deconvolution procedure:

1. We first simulate the fluorescent response by convolution of the two spikes with the kernel (22) $K(t) = A/\tau^2\ te^{-t/\tau}$ where $\tau = 18ms$.
2. To account for possible fluorescence fluctuations, we added a colored noise $\zeta(t)$ that represents fluctuations of the fluorescence signal. The model for the colored noise is an Ornstein-Uhlenbeck process (Schuss, 2009, Chap.1)

$$d\zeta(t) = \mu\zeta(t)dt + \sigma dW(t), \quad \text{(Equation 30)}$$

   where $W(t)$ is a Wiener process and $\mu = 0.045$ and $\sigma = 0.025$. The resulting fluorescence signal is shown Figure S2B (blue). We will then consider this signal as the input of the deconvolution.
3. The deconvolution starts with the fluorescence $A_{rc}(t)$ shown Figure S2C (same as in S2B). Following the deconvolution procedure described above for a single

peak, we approximate the input $A_{rc}(t)$ (Figure S2D (dashed green)), using a sum of exponentials

$$A_{rc}(t) = \sum_{j=0}^{n} \beta_j (t - t_j)^{\alpha_j} e^{-\gamma_j (t - t_j)} \mathrm{H}(t - t_j), \quad \text{(Equation 31)}$$

where the spikes are initiated at time t_j (see Figure S2B, red dashed lines), β_j, $\alpha_j > 2$ and γ_j are positive constants, n is the number of spikes and $\mathrm{H}(t - t_j)$ is the Heaviside function defined by

$$\mathrm{H}(t - t_j) = \begin{cases} 1, & \text{if } t \geq t_j \\ 0, & \text{if } t \geq t_j . \end{cases} \quad \text{(Equation 32)}$$

All parameters are obtained by a fitting procedure.

4. To recover the voltage $V(t)$ from the fluorescence $A_{rc}(t)$, we invert the convolution equation, following the procedure described in the previous section

$$A_{rc}(t) = (V * K)(t) \quad \text{(Equation 33)}$$

We apply the Laplace transform to obtain an analytical representation of the solution

$$\hat{V}(s) = \frac{\hat{A}_{rc}(s)}{\hat{K}(s)} = \sum_{j=0}^{n} \frac{\beta_j \Gamma(\alpha_j + 1)}{A} \frac{(1 + \tau s)^2}{(s + \gamma_j)^{\alpha_j + 1}} e^{-s t_j}. \quad \text{(Equation 34)}$$

5. The voltage $V(t)$ is then recovered computing the inverse Laplace transform of expression (34) and we get

$$V(t) = \sum_{0}^{n} \frac{\beta_j}{A} e^{-\gamma_j (t - t_j)} \mathrm{H}(t - t_j) P_{\tau, \alpha_j, \gamma_j}(t - t_j), \quad \text{(Equation 35)}$$

where

$$P_{\tau, \alpha, \gamma}(t) = t^{\alpha} (\tau\gamma - 1)^2 - 2\alpha\tau(\gamma\tau - 1) t^{\alpha - 1} + \alpha\tau^2(\alpha - 1) t^{\alpha - 2}. \quad \text{(Equation 36)}$$

The deconvolved voltage is shown Figure S2E. Note that the fluctuations disappear completely because the fitting procedure (31) removes them completely. The result of the deconvolution is compared to the initial voltage response (dashed black) in Figure S2F. The deconvolution of the voltage $V(t)$ in step 4 relies on the apriori knowledge of the time of

spike initiation t_j. These values could be identified when the spikes are sufficiently separated: when the time interval between two consecutive peaks $\Delta t_i = t_{i+1} - t_i$ is large enough, the times t_j can be recovered directly from fluorescence measurements: as shown in Figures S2G–S2I for Δt_0 = 75, 100 and 150ms respectively, the two peaks (red star) are clearly distinguishable and the time t_1 can be identified. However, when Δt_0 = 50ms (Figure S2C), the two peaks overlap such that the time t_1 cannot be read from the fluorescence time series but could be identified in the electrophysiology time series.

We conclude that the present deconvolution procedure can be applied to several spikes or EPSP, as long as the time between spikes is not less than $50ms$. When the time between the events is less than $50ms$, the information of their precise position could be retrieved from direct electrophysiological recordings, in that case, the deconvolution procedure still recover the fast time evolution.

Optimization procedure to extract the capacitance C and conductance G of a dendritic spine from the voltage drop between the head and the base of a spine

We describe here an optimization procedure for extracting the capacitance C and conductance G from the measured voltage time series. The procedure consists in fitting a very small portion of the voltage time response curve and to predict from this short time interval, the entire time response. Furthermore, this procedure permits to compute the current $I(t)$ injected in the spine neck, based on Equation 1. We start with the one-dimensional electro-diffusion equations to model the current and voltage in the spine neck. These equations consist of the classical Poisson equation for the voltage and the ionic concentrations coupled to the Fokker-Planck equations for the concentrations and the voltage.

$$\frac{\partial^2 V}{\partial x^2}(x,t) = -\frac{F}{\varepsilon\varepsilon_0}(c_p(x,t) - c_m(x,t)) \qquad \text{(Equation 37)}$$
$$\frac{\partial c_p}{\partial t}(x,t) = D_p \frac{\partial}{\partial x}\left(\frac{\partial c_p}{\partial x}(x,t) + \frac{e}{k_B T} c_p(x,t)\frac{\partial V}{\partial x}(x,t)\right)$$
$$\frac{\partial c_m}{\partial t}(x,t) = D_m \frac{\partial}{\partial x}\left(\frac{\partial c_m}{\partial x}(x,t) - \frac{e}{k_B T} c_m(x,t)\frac{\partial V}{\partial x}(x,t)\right),$$

where D_p, D_m are diffusion coefficients, e the electronic charge, the valencies for each specie is $z = \pm 1$ and $k_B T$ is the thermal energy. Equation 37 is used to compute the voltage drop when a current $I(t)$ is injected at the tip of the spine neck. During the simulations, the ionic concentrations in the dendrite (ionic reservoir) are the boundary conditions fixed at the values C_p and C_m (see Table 2). We recall that the electrical potential is defined to an additive constant. The initial and boundary conditions are

$$V(x,0) = 0 \qquad \text{(Equation 38)}$$

$$c_p(x,0) = C_p \text{ and } c_m(x,0) = C_m.$$

$$\left.\frac{\partial V}{\partial x}(x,t)\right|_{x=0} = 0 \quad \text{(Equation 39)}$$
$$\left.\frac{\partial c_m}{\partial x}(x,t)\right|_{x=0} = 0$$

$$\left.\frac{\partial c_p}{\partial x}(x,t) + \frac{e}{k_B T} c_p(x,t) \frac{\partial V}{\partial x}(x,t)\right|_{x=0} = \frac{I(t)}{D_p F \pi r_i^2},$$

$$V(L,t) = 0,\ c_p(L,t) = C_p \text{ and } c_m(L,t) = C_m, \quad \text{(Equation 40)}$$

where r_i is the radius of the circular opening where the synaptic current is injected in our simulations (see Figure 3A). In summary, Equations 37, 39, and 40 describe the ionic response of an input current $I(t)$ inside a thin cylinder reduced to a one dimensional segment. We simulate these equations using Comsol to determine the voltage drop (Figure 2).

To determine the unknown parameters (C, G), we use an iterative algorithm, where we solve numerically the boundary value problem Equations 37, 38, and 39, from which we obtain a ionic current $I_{C,G}(t)$ (Equation 1) injected at the tip of the neck and the voltage $V_{C,G}(x, t)$ in the neck at position x and at time t. Because $V_{C,G}(L, t) = 0$, the voltage $V_{C,G}(0, t)$ represents the difference of potentials between the head and the dendrite. We start the iteration algorithm with a value for the parameters C_0, G_0: $C_0 = 0.1pF$ and $G_0 = 1nS$ (Figure S4A). Following each iteration, we compare the computed voltage $V_{C,G}(0, t)$ (from Equation 37) with the measured potential difference $V_{head}(t) - V_{dend}(t)$ extracted on a short time interval $[t_i, t_f]$ (usually $[0.2 - 0.4]ms$). We chose this small time window because it allows us differentiating clearly the response from the background noise during glutamate uncaging (Figures S4B–S4D).

The value for the parameters C, G are the minimizers of the error functional—

$$\min_{\{C,G \in S\}} \int_{t_i}^{t_f} |\, V_{C,G}(0,t) - (V_{head}(t) - V_{dend}(t))\,|^2 dt, \quad \text{(Equation 41)}$$

where the ensemble S of parameters is described below. We approximated the difference by a linear function $V_{head}(t) - V_{dend}(t)$

$$\xi(t) = a(t - t_i) + b, \quad \text{(Equation 42)}$$

where a and b are constants fitted to data in the interval $[t_i, t_f]$. This approximation reduces possible fluctuations (see fig. S4B–D). Finally, we score the different couple (C,G) using the estimator

$$S_{C,G} = \sum_{\{t_k \in [t_i, t_f]\}} (V_{C,G}(0, t_k) - \xi(t_k))^2 . \quad \text{(Equation 43)}$$

At the beginning of each iteration, we use possible values for (C, G) among which we retain the optimal values (C^*, G^*) that minimizes the score $S_{C,G}$. The possible values for (C, G) can be represented by a square matrix, centered around the initial value (C_0, G_0), where we have chosen $C_0 = 0.1pF$ and $G_0 = 1nS$ (Koch, 2004). Each couple differs from one another by an increment $\Delta G = 0.05$ and each line and $\Delta C = 0.01$ on each raw. In total, there are $(2\alpha + 1)^2$ values, presented in a matrix

$$\mathrm{S} = \begin{pmatrix} (C + \alpha\Delta C, G - \alpha\Delta G) & \cdots & (C + \alpha\Delta C, G) & \cdots & (C + \alpha dC, G + \alpha\Delta G) \\ \vdots & & \vdots & & \vdots \\ (C, G - \alpha\Delta G) & \cdots & (\mathbf{C}_0, \mathbf{G}_0) & \cdots & (C, G + \alpha\Delta G) \\ \vdots & & \vdots & & \vdots \\ (C - \alpha dC, G - \alpha\Delta G) & \cdots & (C - \alpha\Delta C, G) & \cdots & (C - \alpha dC, G + \alpha\Delta G) \end{pmatrix}. \quad \text{(Equation 44)}$$

We first look for the minimum of expression 43 for all entries of the matrix. For a given precision $(\varepsilon_G, \varepsilon_C)$, we evaluate whether or not the conditions

$$\|C^* - C_0\| < \varepsilon_C \text{ and } \|G^* - G_0\| < \varepsilon_G, \quad \text{(Equation 45)}$$

are satisfied and in that case, we have chosen $V_{C^*,G^*}(x, t) = V(x, t)$, otherwise we continue the iteration by replacing the initial condition with the new values:

$$(C_0, G_0) \leftarrow (C^*, G^*) \quad \text{(Equation 46)}$$

$$(\Delta C, \Delta G) \leftarrow \left(\frac{\Delta C}{2}, \frac{\Delta G}{2}\right). \quad \text{(Equation 47)}$$

This iteration shows how the new 'S' matrix (Equation 45) is refinement near (C^*, G^*). In practice, we always find a unique solution for the final parameter C^* and G^*.

We show in Figure S3 several examples of dendritic spines, where we applied the present algorithm to extract the current, G and C from the voltage deconvolved time series. Figure S3A shows the different region of interest ROIs. In Figure S3B, we compare the deconvolved voltage signal with the one computed from PNP. In Figure S3C, we plot the computed injected current (from voltage) inside the spine neck.

Relation between the intrinsic 1/*G* and the effective neck R_{neck} resistance—We discuss here the relation between the spine effective and intrinsic resistance. The effective neck resistance is computed from the difference of voltage $\langle V(t)\rangle$ between the entrance and the exit of the neck, when the injected current is $\langle I(t)\rangle$. By definition, averaging over time, we have

$$R_{neck} = \frac{\langle V(t)\rangle}{\langle I(t)\rangle}. \quad \text{(Equation 48)}$$

When the injected current follows the model equation

$$I(t) = GV_1(t) + C\frac{dV_1(t)}{dt}, \quad \text{(Equation 49)}$$

where $V_1(t)$ is the voltage in the entrance of the neck, the intrinsic conductance and capacitance are G and C respectively. We thus obtain the following relation with $\langle V(t)\rangle = V_1 - V_2$,

$$R_{neck} = \frac{1}{G + C\frac{d\ln V_1}{dt}(t)}\left(1 - \frac{V_2(t)}{V_1(t)}\right), \quad \text{(Equation 50)}$$

where V_2 is the voltage at the end of the neck. In particular, when $C = 0$,

$$R_{neck} = \frac{1}{G}\left(1 - \frac{V_2(t)}{V_1(t)}\right) < \frac{1}{G}. \quad \text{(Equation 51)}$$

Transient current in a three dimensional spine—We generated a transient current with a timescale of 100 ms (Figures S7A and S7B) from the PNP equations in the geometry consisting of a cylindrical neck plus round head. The equations are given for positive and negative species by

$$\Delta V = \frac{-F}{\varepsilon\varepsilon_0}(c_p - c_m) \quad \text{(Equation 52)}$$

$$\frac{\partial c_p}{\partial t} = D_p \nabla\left(\nabla c_p + \frac{e}{k_B T} c_p \nabla V\right) \quad \text{(Equation 53)}$$

$$\frac{\partial c_m}{\partial t} = D_m \nabla\left(\nabla c_m - \frac{e}{k_B T} c_m \nabla V\right), \quad \text{(Equation 54)}$$

where D_p, D_m are diffusion coefficients, e the electronic charge, the valencies for each specie is $z = \pm 1$ and $k_B T$ is the thermal energy. Note that the electro-neutrality is not necessarily satisfied. Equations 52, 53, and 54 are used to compute the voltage drop when the injected current $I_{stim}(t)$ at the tip of the spine is given by

$$I_{stim}(t) = \frac{I_{\max}}{\tau} t \exp(-t/\tau + 1), \quad \text{(Equation 55)}$$

where $\tau = 100 ms$ is the decay time constant and I_{max} is the maximal current. During the simulations, the ionic concentrations are computed from the boundary conditions:

$$\frac{\partial V}{\partial n} = 0 \text{ on } \partial\Omega_r \cup \partial\Omega_i \quad \text{(Equation 56)}$$

$$\frac{\partial c_p}{\partial n} = \frac{\partial c_p}{\partial n} = 0 \text{ on } \partial\Omega_r$$

$$\frac{\partial c_p}{\partial n} + \frac{e}{k_B T} c_p \frac{\partial V}{\partial n} = \frac{I_{stim}(t)}{\pi r_i^2 F D_p} \text{on } \partial\Omega_i$$

$$\frac{\partial c_m}{\partial n} - \frac{e}{k_B T} c_m \frac{\partial V}{\partial n} = 0 \text{ on } \partial\Omega_i$$

$$V = 0 \text{ on } \partial\Omega_o$$

$$c_p = C_p \text{ on } \partial\Omega_o$$

$$c_m = C_m \text{ on } \partial\Omega_o .$$

We solve Equations 52, 53, 54, 55, and 56 numerically for $I_{max} = 150$ and $300pA$ using Comsol. Results are shown in Figure S7, where we find a concentration gradient at time to peak between the base and the tip of the neck of $\Delta c_p = \Delta c_m = 22mM$ (resp. $45mM$) when $I_{max} = 150pA$ (resp. $300pA$). We conclude that a transient current leads to a gradient of concentration inside a dendritic spine, showing that the assumption of a constant ionic concentration, which is at the basis of the cable equation, is not satisfied.

Three dimensional steady-state PNP-equations in a Ball and a dendritic spine shape—We present now the steady-state PNP equations, that describe the concentration of positive $c_p(\boldsymbol{x})$ and negative $c_m(\boldsymbol{x})$ charge concentrations and the voltage $\phi(\boldsymbol{x})$ inside a three dimensional bounded domain that we use in Figure 3. The equations are given by

$$\Delta\phi(\boldsymbol{x}) = \frac{-F}{\varepsilon\varepsilon_0}(c_p(\boldsymbol{x}) - c_m(\boldsymbol{x})) \qquad \text{(Equation 57)}$$
$$0 = D_p \nabla\left(\nabla c_p(\boldsymbol{x}) + \frac{e}{k_B T} c_p \nabla\phi(\boldsymbol{x})\right)$$
$$0 = D_m \nabla\left(\nabla c_m(\boldsymbol{x}) - \frac{e}{k_B T} c_m \nabla\phi(\boldsymbol{x})\right).$$

The boundary is decomposed into three subdomains: the current is injected into $\partial\Omega_i$. Charges can exit in $\partial\Omega_o$ and the impermeable membrane is represented by $\partial\Omega_r$. The boundary conditions are

$$\frac{\partial\phi}{\partial n}(\boldsymbol{x}) = 0 \text{ on } \partial\Omega_r \cup \partial\Omega_i \qquad \text{(Equation 58)}$$
$$\frac{\partial c_p}{\partial n}(\boldsymbol{x}) = \frac{\partial c_p}{\partial n}(\boldsymbol{x}) = 0 \text{ on } \partial\Omega_r$$
$$\frac{\partial c_p}{\partial n}(\boldsymbol{x}) + \frac{e}{k_B T} c_p(\boldsymbol{x}) \frac{\partial\phi}{\partial n}(\boldsymbol{x}) = \frac{I_{stim}}{\pi r_i^2 F D_p} \text{on } \partial\Omega_i$$
$$\frac{\partial c_m}{\partial n}(\boldsymbol{x}) - \frac{e}{k_B T} c_m(\boldsymbol{x}) \frac{\partial\phi}{\partial n}(\boldsymbol{x}) = 0 \text{ on } \partial\Omega_i$$

$$\phi(\boldsymbol{x}) = 0 \text{ on } \partial\Omega_o$$

$$c_p(\boldsymbol{x}) = C_p \text{ on } \partial\Omega_o$$

$$c_m(\boldsymbol{x}) = C_m \text{ on } \partial\Omega_o .$$

In that model, only positive charges can enter the spine domain. We use the Comsol platform to solve numerically Equation 57, presented and discussed in Figure 3.

Computing the neck resistance for long spines—We computed the spine neck resistance $R_{neck} = \langle V_{head} \rangle / I_{stim}$ (Figure S7D) from the simulations of the PNP Equation 57 with boundary conditions (58) with the new parameter values for the neck length $L = 1\mu m$ (typical for culture hippocampal neurons) versus $L = 2\mu m$ (slices). We find that the neck resistance is small for shorter spine (culture hippocampal neurons) compared to brain slices. Indeed, by doubling the neck length the neck resistance increases from $117M\Omega$ to $203M\Omega$. However, the most sensitive parameter is the neck radius which remains unaccessible. Reducing the neck radius from 100 to $50nm$ in both cases of $L = 1$ (resp. $L = 2\mu m$) increases the neck resistance from $117M\Omega$ to $339M\Omega$ (resp. from $203M\Omega$ to $518M\Omega$).

Limitation of the cable theory—To confirm the limitation of the cable theory in describing the potential change across the spine neck, we use the cable Equation 60 below for the potential $V(x, t)$ at position x and time t along a one dimensional segment (Koch, 2004). We impose a first condition for the voltage at the entrance of the spine neck from the head $V(0, t) = V_{head}(t)$, while the boundary condition at $x = L$ assumes a zero electric field at the connection with the dendrite. We use for $V_{head}(t)$ the deconvolved voltage measured in the head.

The diffusion equation for voltage is

$$\tau \frac{\partial V(x,t)}{\partial t} = \lambda^2 \frac{\partial^2 V(x,t)}{\partial x^2} - V(x,t) \quad \text{(Equation 59)}$$

$$V(0,t) = V_1(t) \quad \text{(Equation 60)}$$

$$\left.\frac{\partial V(x,t)}{\partial x}\right|_{x=L} = 0. \quad \text{(Equation 61)}$$

where the two independent parameters $\lambda = \sqrt{r_m / r_a}$ and $\tau = r_m c_m$ (Koch, 2004, Chapter 2) are related to the membrane capacitance c_m, the resistance r_m and the intracellular resistance r_a. By definition, $r_m = R_m / \pi d$ and $c_m = C_m \cdot \pi d$, where R_m is the specific membrane resistance and C_m the specific membrane capacitance and d is the diameter of the cable (Koch, 2004).

Voltage changes computed from the cable model (green dashed) when the input is the measured voltage in the head (blue) does not match the measured response in the dendrite (red). To obtain a response comparable to the output, the intracellular resistivity should be increased by a factor 3.10^5, showing the limitation of the cable equation to account for the voltage propagation in a dendritic spine (Figure S6).

We recall that the cable theory is an approximation derived the 1D Nernst-Planck equations (Koch, 2004, p. 261) that assumes there is no concentration fluctuations along the cable:

$\partial c_i(x, t)/\partial x = 0$. However as pointed out in (Koch, 2004, p. 28), within a compartment with a small diameter ($<1\mu m$) the concentration should vary: $\partial c_i(x, t)/\partial x \neq 0$. We found using numerical simulations of PNP in the neck that the longitudinal concentration is not zero. Indeed, as shown in the main text Figure 4D and in Figure S7, we have $\partial c_i(x, t)/\partial x \approx 50\ mM\mu m^{-1} \neq 0$.

Furthermore, the cable theory predicts a decay of the voltage characterized by a space constant

$$\lambda = \sqrt{\frac{R_m d}{4R_i}}, \quad \text{(Equation 62)}$$

where d is the diameter of the cable, R_m the membrane capacitance and R_i the intracellular resistivity. It characterizes the exponential decay of the voltage along an infinite cable such that $V(x) = V_{init} e^{-|x|/\lambda}$ (Koch, 2004, p. 32). Consequently, at a distance λ the initial voltage V_{init} is decreased of e^{-1} (36.7%). For example, choosing $R_m = 2 \cdot 10^4\ \Omega cm^2$, $R_i = 200\ \Omega cm$ we have $\lambda = 1mm$ for a $4\mu m$ thick dendrite (Koch, 2004). A spine neck radius of $100nm$ or $50nm$ gives $\lambda = 220\mu m$ and $160\mu m$ respectively. However, the data of the voltage transduction in the spine neck (Figure S3) shows that more than 50% of the voltage amplitude is attenuated in a neck of length $L = 1\mu m \ll \lambda$. The present analysis confirms that the cable theory cannot be used to predict the electrical behavior of a dendritic spine (Qian and Sejnowski, 1989; Koch, 2004).

Modeling the spine membrane capacitance—To account for the possible effect of the membrane capacitance in our model, we modified the boundary condition in the Poisson equation

$$\frac{\partial V(\boldsymbol{x}, t)}{\partial n} = 0 \text{ on } \partial\Omega_r \quad \text{(Equation 63)}$$

to (Feynman et al., 2005, Chapter 6)

$$\frac{\partial V(\boldsymbol{x}, t)}{\partial n} = \varepsilon_r \frac{V_{ext} - V(\boldsymbol{x}, t)}{d} \text{on } \partial\Omega_r. \quad \text{(Equation 64)}$$

where V_{ext} is the extracellular voltage (assumed fixed at 65mV). The constants $\varepsilon_r = 5$ and $d = 8nm$ are the membrane relative permitivity and thickness respectively (Ashrafuzzaman and Tuszynski, 2012, Chapter 2) (Figure S5A).

We simulate the voltage V near the membrane and in the bulk for a steady-current $I = 50pA$. We compare the two voltages obtained numerically for each condition (63) and (64 s). The

difference between the mean voltages was less than <1.5% (Figure S5B) and the axial (bulk) voltages by accounting or not for the capacitance, only differs from 0.015% (Figure S5C). We conclude that the neck capacitance can be neglected and the reflecting boundary condition $\partial V/\partial n = 0$ that we imposed is a good enough approximation.

DATA AND SOFTWARE AVAILABILITY

The PNP equations were solved using the finite element method implemented in the software COMSOL Multiphysics. We used the default MUltifrontal Massively Parallel solver (MUMPS). We applied an adaptive mesh refinement to eliminate mesh dependency. Any time-derivative functions were approximated by a n^{th} order backward differentiation formulas, $n \in [|1, 3|]$, where the maximal time-step is $dt = 5{\cdot}10^{-3}s$. The convergence of the method was ensured by setting an absolute tolerance at 0.001.

The optimization and filtering procedures were performed using the software MATLAB 2015. The numerical codes are available on our platform http://www.bionewmetrics.org.

Supplementary Material

Refer to Web version on PubMed Central for supplementary material.

Acknowledgments

D.H. thanks the hospitality of Department of Applied Mathematics and Theoretical Physics (DAMTP), Churchill College CB3 0DS; this work is supported by a Simons fellowship Award. This research is supported by a Equipes FRM 2016 grant (DEQ20160334882). R.Y. and T.K. are supported by the NIMH (R01MH101218, R01-MH100561). This material is based upon work supported by, or in part by, the U.S. Army Research Laboratory and the U.S. Army Research Office under contract number W911NF-12-1-0594 (MURI).

References

Abramowitz, M., Stegun, IA. Applied Mathematics Series. Vol. 55. Dover Publications; 1966. Handbook of Mathematical Functions.

Acker CD, Hoyos E, Loew LM. Epsps measured in proximal dendritic spines of cortical pyramidal neurons. eNeuro. 2016; 3 ENEURO.0050-15.2016.

Araya R, Jiang J, Eisenthal KB, Yuste R. The spine neck filters membrane potentials. Proc Natl Acad Sci USA. 2006; 103:17961–17966. [PubMed: 17093040]

Araya R, Vogels TP, Yuste R. Activity-dependent dendritic spine neck changes are correlated with synaptic strength. Proc Natl Acad Sci USA. 2014; 111:E2895–E2904. [PubMed: 24982196]

Ashrafuzzaman, M., Tuszynski, JA. Membrane Biophysics. Springer Science & Business Media; 2012.

Beaulieu-Laroche L, Harnett MT. Dendritic spines prevent synaptic voltage clamp. Neuron. 2018; 97:75–82e3. [PubMed: 29249288]

Bezanilla F. How membrane proteins sense voltage. Nat Rev Mol Cell Biol. 2008; 9:323–332. [PubMed: 18354422]

Bloodgood BL, Sabatini BL. Neuronal activity regulates diffusion across the neck of dendritic spines. Science. 2005; 310:866–869. [PubMed: 16272125]

Brinks D, Klein AJ, Cohen AE. Two-photon lifetime imaging of voltage indicating proteins as a probe of absolute membrane voltage. Biophys J. 2015; 109:914–921. [PubMed: 26331249]

Chen KC, Nicholson C. Spatial buffering of potassium ions in brain extracellular space. Biophys J. 2000; 78:2776–2797. [PubMed: 10827962]

Crick F. Do dendritic spines twitch? Trends Neurosci. 1982; 5:44–46.

Eisenberg RS. From structure to function in open ionic channels. J Membr Biol. 1999; 171:1–24. [PubMed: 10485990]

Eisenberg RS. Look at biological systems through an engineer's eyes. Nature. 2007; 447:376–376.

Eisenberg R, Klosek M, Schuss Z. Diffusion as a chemical reaction: Stochastic trajectories between fixed concentrations. J Chem Phys. 1995; 102:1767–1780.

Elias GM, Nicoll RA. Synaptic trafficking of glutamate receptors by MAGUK scaffolding proteins. Trends Cell Biol. 2007; 17:343–352. [PubMed: 17644382]

Emiliani V, Cohen AE, Deisseroth K, Häusser M. All-optical interrogation of neural circuits. J Neurosci. 2015; 35:13917–13926. [PubMed: 26468193]

Feynman, R., Leighton, R., Sands, M. The Feynman Lectures on Physics, Volume ii: Mainly Electromagnetism and Matter. Pearson; 2005.

Gong Y, Huang C, Li JZ, Grewe BF, Zhang Y, Eismann S, Schnitzer MJ. High-speed recording of neural spikes in awake mice and flies with a fluorescent voltage sensor. Science. 2015; 350:1361–1366. [PubMed: 26586188]

Han Z, Jin L, Platisa J, Cohen LB, Baker BJ, Pieribone VA. Fluorescent protein voltage probes derived from ArcLight that respond to membrane voltage changes with fast kinetics. PLoS ONE. 2013; 8:e81295. [PubMed: 24312287]

Han Z, Jin L, Chen F, Loturco JJ, Cohen LB, Bondar A, Lazar J, Pieribone VA. Mechanistic studies of the genetically encoded fluores-cent protein voltage probe ArcLight. PLoS ONE. 2014; 9:e113873. [PubMed: 25419571]

Harnett MT, Makara JK, Spruston N, Kath WL, Magee JC. Synaptic amplification by dendritic spines enhances input cooperativity. Nature. 2012; 491:599–602. [PubMed: 23103868]

Herring BE, Nicoll RA. Long-term potentiation: from camkii to ampa receptor trafficking. Annu Rev Physiol. 2016; 78:351–365. [PubMed: 26863325]

Hille, B. Ion Channels of Excitable Membranes. Sinauer; 2001.

Hochbaum DR, Zhao Y, Farhi SL, Klapoetke N, Werley CA, Kapoor V, Zou P, Kralj JM, Maclaurin D, Smedemark-Margulies N, et al. All-optical electrophysiology in mammalian neurons using engineered microbial rhodopsins. Nat Methods. 2014; 11:825–833. [PubMed: 24952910]

Holcman D, Schuss Z. Control of flux by narrow passages and hidden targets in cellular biology. Rep Prog Phys. 2013; 76:074601. [PubMed: 23787818]

Holcman D, Yuste R. The new nanophysiology: regulation of ionic flow in neuronal subcompartments. Nat Rev Neurosci. 2015; 16:685–692. [PubMed: 26462753]

Holmes WR, Segev I, Rall W. Interpretation of time constant and electrotonic length estimates in multicylinder or branched neuronal structures. J Neurophysiol. 1992; 68:1401–1420. [PubMed: 1432089]

Horowitz, P., Hill, W. The Art of Electronics. Cambridge University Press; 1989.

Huganir RL, Nicoll RA. AMPARs and synaptic plasticity: the last 25 years. Neuron. 2013; 80:704–717. [PubMed: 24183021]

Jack, JJB., Noble, D., Tsien, RW. Electric Current Flow in Excitable Cells. Oxford University Press; 1975.

Jackson, JD. Classical Electrodynamics. John Wiley & Sons; 2007.

Jayant K, Hirtz JJ, Plante IJ, Tsai DM, De Boer WD, Semonche A, Peterka DS, Owen JS, Sahin O, Shepard KL, Yuste R. Targeted intracellular voltage recordings from dendritic spines using quantum-dot-coated nanopipettes. Nat Nanotechnol. 2017; 12:335–342. [PubMed: 27941898]

Jin L, Han Z, Platisa J, Wooltorton JR, Cohen LB, Pieribone VA. Single action potentials and subthreshold electrical events imaged in neurons with a fluorescent protein voltage probe. Neuron. 2012; 75:779–785. [PubMed: 22958819]

Kessels HW, Malinow R. Synaptic AMPA receptor plasticity and behavior. Neuron. 2009; 61:340–350. [PubMed: 19217372]

Koch, C. Biophysics of Computation: Information Processing in Single Neurons. Oxford University Press; 2004.

Koch, C., Segev, I. Methods in Neuronal Modeling: From Ions to Networks. MIT Press; 1998.

Korkotian E, Segal M. Regulation of dendritic spine motility in cultured hippocampal neurons. J Neurosci. 2001a; 21:6115–6124. [PubMed: 11487635]

Korkotian E, Segal M. Spike-associated fast contraction of dendritic spines in cultured hippocampal neurons. Neuron. 2001b; 30:751–758. [PubMed: 11430808]

Korkotian E, Holcman D, Segal M. Dynamic regulation of spine-dendrite coupling in cultured hippocampal neurons. Eur J Neurosci. 2004; 20:2649–2663. [PubMed: 15548208]

Kwon T, Sakamoto M, Peterka DS, Yuste R. Attenuation of synaptic potentials in dendritic spines. Cell Rep. 2017; 20:1100–1110. [PubMed: 28768195]

Lopreore CL, Bartol TM, Coggan JS, Keller DX, Sosinsky GE, Ellisman MH, Sejnowski TJ. Computational modeling of three-dimensional electrodiffusion in biological systems: application to the node of Ranvier. Biophys J. 2008; 95:2624–2635. [PubMed: 18556758]

McLaughlin S, Poo MM. The role of electro-osmosis in the electric-field-induced movement of charged macromolecules on the surfaces of cells. Biophys J. 1981; 34:85–93. [PubMed: 6894257]

Nicoll RA. A brief history of long-term potentiation. Neuron. 2017; 93:281–290. [PubMed: 28103477]

Peterka DS, Takahashi H, Yuste R. Imaging voltage in neurons. Neuron. 2011; 69:9–21. [PubMed: 21220095]

Pnevmatikakis EA, Soudry D, Gao Y, Machado TA, Merel J, Pfau D, Reardon T, Mu Y, Lacefield C, Yang W, et al. Simultaneous denoising, deconvolution, and demixing of calcium imaging data. Neuron. 2016; 89:285–299. [PubMed: 26774160]

Popovic MA, Carnevale N, Rozsa B, Zecevic D. Electrical behaviour of dendritic spines as revealed by voltage imaging. Nat Commun. 2015; 6:8436. [PubMed: 26436431]

Qian N, Sejnowski T. An electro-diffusion model for computing membrane potentials and ionic concentrations in branching dendrites, spines and axons. Biol Cybern. 1989; 62:1–15.

Savitzky A, Golay MJ. Smoothing and differentiation of data by simplified least squares procedures. Anal Chem. 1964; 36:1627–1639.

Savtchenko LP, Kulahin N, Korogod SM, Rusakov DA. Electric fields of synaptic currents could influence diffusion of charged neuro-transmitter molecules. Synapse. 2004; 51:270–278. [PubMed: 14696014]

Savtchenko LP, Poo MM, Rusakov DA. Electrodiffusion phenomena in neuroscience: a neglected companion. Nat Rev Neurosci. 2017; 18:598–612. [PubMed: 28924257]

Schuss, Z. Theory and Applications of Stochastic Processes: An Analytical Approach. Vol. 170. Springer Science & Business Media; 2009.

St-Pierre F, Marshall JD, Yang Y, Gong Y, Schnitzer MJ, Lin MZ. High-fidelity optical reporting of neuronal electrical activity with an ultrafast fluorescent voltage sensor. Nat Neurosci. 2014; 17:884–889. [PubMed: 24755780]

Strathmann, H. Ion-Exchange Membrane Separation Processes. Vol. 9. Elsevier; 2004.

Svoboda K, Denk W, Kleinfeld D, Tank DW. In vivo dendritic calcium dynamics in neocortical pyramidal neurons. Nature. 1997; 385:161–165. [PubMed: 8990119]

Sylantyev S, Savtchenko LP, Niu YP, Ivanov AI, Jensen TP, Kullmann DM, Xiao MY, Rusakov DA. Electric fields due to synaptic currents sharpen excitatory transmission. Science. 2008; 319:1845–1849. [PubMed: 18369150]

Sylantyev S, Savtchenko LP, Ermolyuk Y, Michaluk P, Rusakov DA. Spike-driven glutamate electrodiffusion triggers synaptic potentiation via a homer-dependent mGluR-NMDAR link. Neuron. 2013; 77:528–541. [PubMed: 23395378]

Takasaki KT, Ding JB, Sabatini BL. Live-cell superresolution imaging by pulsed STED two-photon excitation microscopy. Biophys J. 2013; 104:770–777. [PubMed: 23442955]

Tønnesen J, Katona G, Rózsa B, Nägerl UV. Spine neck plasticity regulates compartmentalization of synapses. Nat Neurosci. 2014; 17:678–685. [PubMed: 24657968]

Tsodyks MV, Markram H. The neural code between neocortical pyramidal neurons depends on neurotransmitter release probability. Proc Natl Acad Sci USA. 1997; 94:719–723. [PubMed: 9012851]

Yuste, R. Dendritic Spines. MIT Press; 2010.

Highlights

- Deconvolution of fluorescence Arclight to recover voltage in dendritic spines
- The voltage distribution in spines modulated by geometry and electro-diffusion
- A concentration gradient appears in the spine neck following a synaptic input
- Spine electrical resistance depends on the injected current, Ohm's law not valid

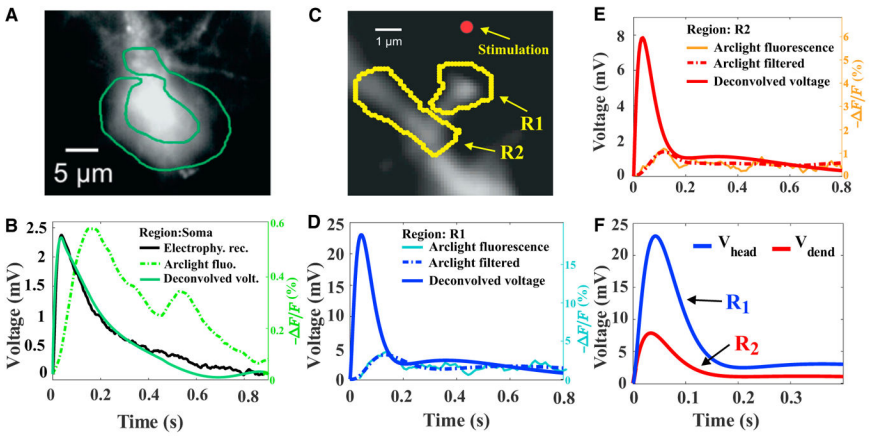

Figure 1. Voltage Drop across a Dendritic Spine Measured from Arclight

(A) A region of interest is selected around the soma to estimate the fluorescence during a synaptic stimulation.

(B) The deconvolution of the fluorescence signal (dashed green) in the soma uses the electrophysiological recording (continuous black) to obtain the deconvolved voltage (continuous green) (we refer also to Figures S1C–S1E for further details on the filtering procedure). Fluorescence and electrophysiology are both traces averaged over 6 spines (Figure S3 for 5 other examples).

(C) Regions of interest (ROIs) *R*1 and *R*2 representing the spine and the dendrite, respectively. The red dot shows the location where glutamate is uncaged.

(D and E) Deconvolution of the fluorescence signal (single trial) in the dendritic spine *R*1 (D) and the dendrite *R*2 (E) using the kernel $K(t)$ found in the soma deconvolution in (see B).

(F) Comparison of the filtered and deconvolved voltage signal in the spine head and parent dendrite.

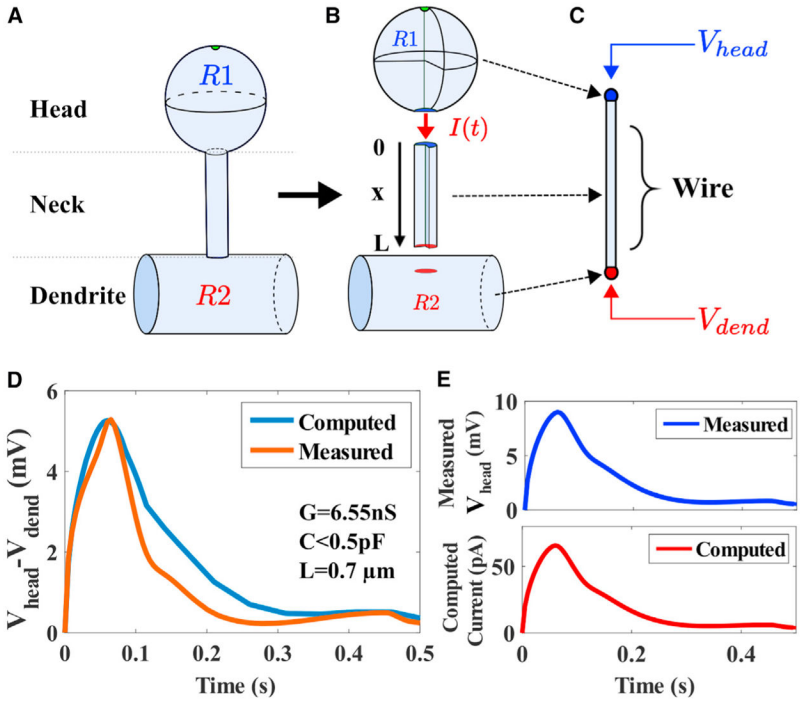

Figure 2. Extracting the Electrical Parameters of a Dendritic Spine from a Reduced Model and Voltage Dynamics

(A and B) Schematic representation of a dendritic spine, divided into three regions: the head *R*1, the neck of length *L*, and the close dendrite *R*2. The current *I*(*t*) represents the axial current escaping from the head to the dendrite.

(C) Reduced geometry of a dendritic spine neck of length *L*, approximated as a dielectric wire. The input is the measured voltage $V_{head}(t)$ of ROIs (Figure 1C) *R*1 at the head ($x = 0$) and we use voltage $V_{dend}(t)$ (*R*2) in the parent dendrite ($x = L$) as an output for comparison with the numerical computation.

(D) Comparison of measured (trace averaged over 6 spines) (orange) and computed (blue) voltages. The parameters *C* and *G* are used in (1) to estimate the injected current.

(E) Measured membrane potential (blue) in the spine head is used to compute the ionic current (red) from (1), after the parameters (*C*, *G*) are extracted from the iterative method developed in the STAR Methods.

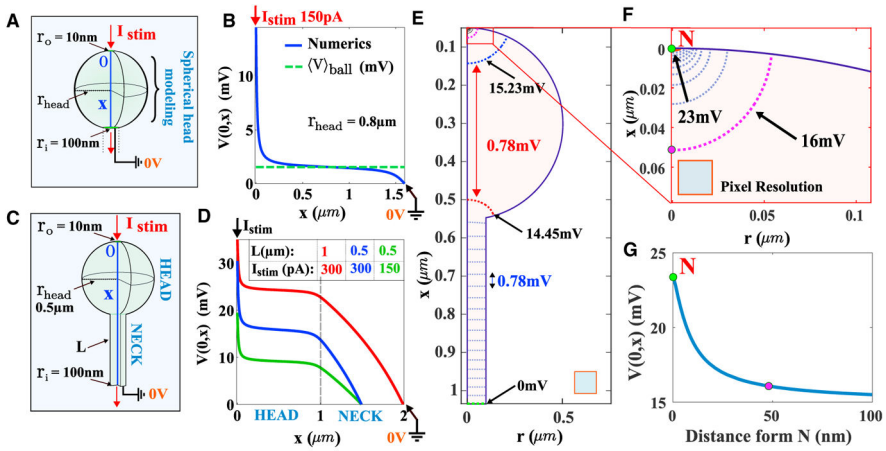

Figure 3. Simulation of PNP Equations for Electro-diffusion in a Dendritic Spine

(A) Representation of a spine head where a current is injected in a 3D spherical cavity of radius $r_{head} = 0.5\mu m$.

(B) Voltage profile (blue) along the x axis obtained from three-dimensional simulations of the PNP equations that we compare to the potential averaged over the entire head (dashed green line) when the injected current is $I_{stim} = 150pA$. The south pole is grounded at $V = 0\,V$.

(C) Representation of a 3D spine geometry composed by a spherical head of radius $r_{head} = 0.5\mu m$ and a neck of length $L = 1\mu m$. The head has two narrow openings, one of radius $10nm$ where the steady current I_{stim} is injected (north) and a second one (south) of $100nm$ at the junction with the neck.

(D) Potential drop along the x axis computed from the top of the head to the bottom of the spine. We compare the voltage drop between a spine where $L = 1\mu m$ and $I_{stim} = 300pA$ (red) with $L = 0.5\mu m$ and $I_{stim} = 150pA$ (blue).

(E) Voltage isolines in a longitudinal cross-section of a spine-like geometry.

(F) Magnification near the north pole N where the current is injected.

(G) Voltage in the neighborhood of the north pole N, computed in 100 nm along the z axis.

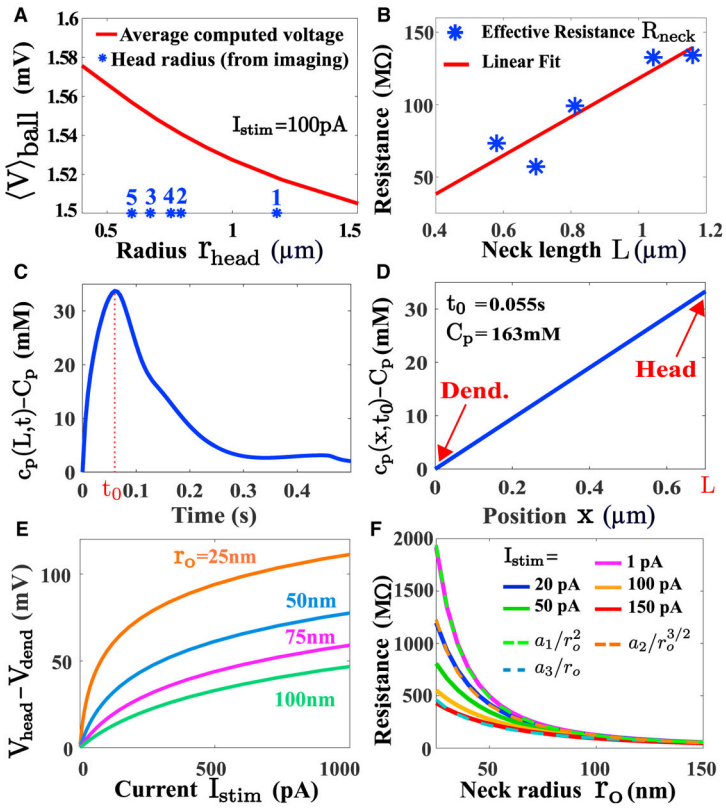

Figure 4. Electrical Properties of Dendritic Spines

(A) Averaged voltage computed in a spine head using PNP (see Figure 3B): for various head radius, the voltage is almost constant ($\langle V\rangle_{ball} \in [1.52, 1.56] mV$). The stars (blue) correspond to the radii of different spine heads based of their surface, determined from one photon image. The indexes refer to the different spines in Table 1. (B) Estimated spine neck resistance (blue stars) computed as the ratio of the voltage to the current averaged over the time responses $R_{neck} = \langle V(0, t)\rangle / \langle I(t)\rangle$ for 5 different spines, revealing how the spine resistance depends on the neck length.

(C) PNP simulation showing the concentration of positive charges at the end of the neck for the injected current described in Figure 2E. The response peaks at $t_0 = 0.055s$.

(D) Distribution of charges at the peak, computed from PNP, showing a large concentration difference of 33 mM (the total concentration 163 mM).

(E) Predicted I–V relation in a dendritic spine for different spine neck radius.

(F) The spine neck resistance is defined by the ratio $R_{neck} = \langle V\rangle_{head} / I_{stim}$. The neck length is $L = 1\mu m$ and a radius $r_{head} = 0.5\mu m$. The different injected current $I_{stim} = 20; 50; 100; 150 pA$. The averaged voltage in the head $\langle V\rangle_{head}$ is computed from system of PNP Equation 57. The computed resistance R_{neck} is fitted to power laws a_1/r_o^2 (dashed green) and $a_2/r_o^{3/2}$ (dashed orange) and a_3/r_o (dashed blue) where $a_1 = 1.23 \cdot 10^6$ $a_2 = 1.57 \cdot 10^5$ and $a_3 = 1.22 \cdot 10^4$.

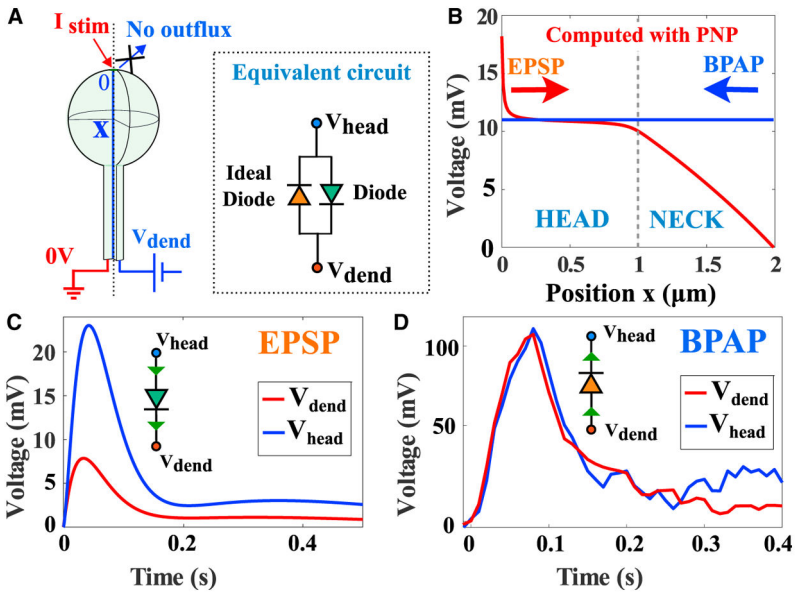

Figure 5. Summary of Dendritic Spine Electrical Responses

(A) Schematic representation of a dendritic spine. Left: a current is injected in the head. Right: modeling the effect of the BPAP on the spine voltage. The inset is an electrical circuit representation of the spine electrical properties, composed by a diode (green) with a resistance R_{neck} in the direction spine to dendrite and by ideal diode in the opposite direction (orange).

(B) Electrical response of a spine (length and radius of the head are $L = R = 1\mu m$) and the radius of the neck $r_0 = 0.1\mu m$, following a synaptic input ($I_{stim} = 100pA$) and a BPAP, where the value depends on the voltage in the dendrite, but it is constant in the spine.

(C) Modulation of the voltage between the spine head and the dendrite: the voltage attenuation can be modeled as a diode to account for the saturation behavior (Figure 3F).

(D) Response to a BPAP showing no voltage change between the head and the dendrite, as predicted by the electro-diffusion model.

Table 1

Extracted Parameters from Modeling

Spine	Neck Length L (μm)	Head Radius r_{head} (μm)	Intrinsic Capa. C (pF)	Intrinsic Res. 1/G ($M\Omega$)	Effective Neck Res. R_{neck} ($M\Omega$)
1	0.6	1.2	<0.5	128.5	73.3
2	0.7	0.8	<0.5	163.4	57.1
3	0.8	0.7	18	212	99.15
4	1.0	0.8	10	252	132.6
5	1.2	0.6	<0.5	261	134.1

Columns 1: spine indices. Column 2: neck length L. Column: 3 radius r_{head} of the spine head computed using formula 2. Column 4: intrinsic capacitance C (section 2 of the SI). Column 5: Intrinsic resistance of the spine $1/G$ (section 2 of the SI). Column 6: spine neck resistance, computed from formula $R_{neck} = \langle V(0, t) - V(L, t)\rangle / \langle I(t)\rangle$ (see section S3 for the definition and computation), where V(0,t) and V(L,t) represent the voltage at 0 (entrance of the neck) and L (based of the spine) respectively and $\langle\cdot\rangle$represents the time averaging between 0 and 0.5 s. We computed V(0,t) and V(L,t) from formula 9 and the current I(t) from Equation 1.

Table 2

Biophysical and Geometrical Parameters

Parameter	Description	Value
z	Valence of ions	1
D	Diffusion coeffcient	200 $\mu m^2/s$ (Chen and Nicholson, 2000)
D_p	Diff. coeff. for + charges	D
D_m	Diff. coeff. for − charges	D
C_p	+ charge concentration	167 mol/m^3 (Hille, 2001, Chapter 1)
C_m	− charge concentration	167 mol/m^3 (Hille, 2001, Chapter 1)
Ω	Spine head	Ω (volume $\|\Omega\|$ ≈1fL) (Yuste, 2010, Chapter 3)
r_o	Spine neck radius	(typical) 0.1 μm (Takasaki et al., 2013)
L	Spine neck length	(typical) 1 μm
T	Temperature	293.15K
E	Energy	kT = 2.58·10^{-2} eV
e	Electron charge	1.6·10^{-19} C
ε	Dielectric constant	ε = 80
ε_0	Abs. Dielectric constant	8.8·10^{-12} F/m
k	Boltzmann constant	1.38·10^{-23} J/K
F	Faraday constant	96, 485 As/mol